NEOPLASIA
www.neoplasia.com

Volume 15 Number 11 November 2013 pp. 1241–1250 1241

Mapping *In Vivo* Tumor Oxygenation within Viable Tumor by ^{19}F-MRI and Multispectral Analysis[1]

Yunzhou Shi*, Jason Oeh†, Jeffrey Eastham-Anderson‡, Sharon Yee†, David Finkle†, Franklin V. Peale Jr‡, Jed Ross*, Maj Hedehus*, Nicholas van Bruggen*, Rayna Venook†, Sarajane Ross†, Deepak Sampath† and Richard A. D. Carano*

*Department of Biomedical Imaging, Genentech Inc, South San Francisco, CA; †Department of Translational Oncology, Genentech Inc, South San Francisco, CA; ‡Department of Pathology, Genentech Inc, South San Francisco, CA

Abstract

Quantifying oxygenation in viable tumor remains a major obstacle toward a better understanding of the tumor microenvironment and improving treatment strategies. Current techniques are often complicated by tumor heterogeneity. Herein, a novel *in vivo* approach that combines ^{19}F magnetic resonance imaging (^{19}F-MRI) R_1 mapping with diffusion-based multispectral (MS) analysis is introduced. This approach restricts the partial pressure of oxygen (pO_2) measurements to viable tumor, the tissue of therapeutic interest. The technique exhibited sufficient sensitivity to detect a breathing gas challenge in a xenograft tumor model, and the hypoxic region measured by MS ^{19}F-MRI was strongly correlated with histologic estimates of hypoxia. This approach was then applied to address the effects of antivascular agents on tumor oxygenation, which is a research question that is still under debate. The technique was used to monitor longitudinal pO_2 changes in response to an antibody to vascular endothelial growth factor (B20.4.1.1) and a selective dual phosphoinositide 3-kinase/mammalian target of rapamycin inhibitor (GDC-0980). GDC-0980 reduced viable tumor pO_2 during a 3-day treatment period, and a significant reduction was also produced by B20.4.1.1. Overall, this method provides an unprecedented view of viable tumor pO_2 and contributes to a greater understanding of the effects of antivascular therapies on the tumor's microenvironment.

Neoplasia (2013) 15, 1241–1250

Introduction

Regional hypoxia is one of the most important factors regulating tumor growth as well as influencing the clinical outcome after therapeutic intervention [1,2]. Assessing tumor regional hypoxia quantitatively, both spatially and temporally, is challenging because of the need for a noninvasive technique and the complications arising from heterogeneity in tumor morphometry. A number of techniques have been developed in an effort to better visualize tumor hypoxia, either by detecting the presence of hypoxic cells or quantitatively measuring the partial pressure of oxygen (pO_2) [3]. Hypoxic cells can be detected immunohistochemically or by positron emission tomography in which 2-nitroimidazole–like imaging markers covalently bind to hypoxic cells. However, these methods are single time-point measurements and are dependent on a biochemical reaction. Direct pO_2 measurements can be achieved by several techniques that each face individual limitations: polarographic electrodes invasively measure oxygenation in the local tissue around the electrode; optical measurements are severely limited by penetration depth; Overhauser imaging and electron paramagnetic resonance imaging are not as readily available to most research groups as alternative imaging approaches, such as magnetic resonance imaging (MRI) [3]. ^{19}F-MRI oximetry [4–7], which uses perfluorocarbon (PFC) emulsions as an imaging contrast agent, is a noninvasive method that can map tumor pO_2 *in vivo*. Compared to ^{1}H-MRI pO_2 techniques [8,9], ^{19}F-MRI has no background signal resulting in a pO_2 signal that is specific to the contrast agent. Given that PFCs are well tolerated in animals and are highly stable in tissue,

Address all correspondence to: Richard A. D. Carano, PhD, Genentech, Inc, MS-228, 1 DNA Way, South San Francisco, CA 94080. E-mail: carano.richard@gene.com

[1]This article refers to supplementary materials, which are designated by Figures W1 and W2 and are available online at www.neoplasia.com.

Received 14 August 2013; Revised 16 October 2013; Accepted 21 October 2013

DOI 10.1593/neo.131468

the use of PFCs allows repeated measurements [10]. The underlying principle is that the spin-lattice, or longitudinal, relaxation rate (R_1) of certain PFCs is a linear function of oxygen levels at a given temperature. Therefore, the power of ^{19}F-MRI oximetry is that the pO_2 measurement is independent of the absolute ^{19}F signal intensity (PFC uptake). Taken together, ^{19}F-MRI can provide a direct noninvasive oxygen measurement [4–7].

Unfortunately, all of these attempts to measure tumor oxygenation suffer from the confounding effects of tumor heterogeneity. Regional hypoxia, associated with the spatial heterogeneity of tumor perfusion and metabolism, contributes to the heterogeneous tissue morphology of solid tumors [2,11]. Tumor heterogeneity can complicate the quantification of tissue pO_2 for a number of reasons, including the following: sampling errors associated with point measurements (e.g., polarographic electrodes), variability in the distribution of the contrast agent, and the inclusion of nonviable tumor regions in whole-tumor estimates. To address tumor heterogeneity, Carano et al. developed a diffusion-based multispectral (MS) technique to distinguish regions of viable tumor, necrosis, and subcutaneous adipose tissue based on the apparent diffusion coefficient (ADC), spin-spin relaxation time (T_2), and proton density (M_0) [12]. Specifically, the viable tumor, the tissue of therapeutic interest, was previously found to be well correlated with a histologic estimate of viable tumor [12].

A novel approach that combines ^{19}F-MRI R_1 mapping with a diffusion-based MS analysis approach as a means to spatially map *in vivo* pO_2 in the viable tumor, the tissue of therapeutic interest, is presented in this manuscript. Using a breathing gas challenge experiment, it is shown that pO_2 measurements can be restricted to the viable tumor, the most relevant area of the tumor rather than including the necrotic areas as occurs with whole-tumor estimates.

The ultimate goal of developing this approach is to study hypoxia in the tissue of therapeutic interest (viable tumor) during tumor progression and to monitor the response to treatments. Specifically, the effects of antivascular agents on tumor oxygenation have been in question for a number of years, where differing responses for tumor pO_2 have been reported [11,13–16]. To address this question, an antibody that blocks both murine and human vascular endothelial growth factor A (VEGF-A; B20.4.1.1) was evaluated by MS ^{19}F-MRI. B20.4.1.1 has been previously shown to reduce vascular density [17] and, thus, may alter O_2 supply through this mechanism. Furthermore, a novel dual phosphoinositide 3-kinase (PI3K)/mammalian target of rapamycin (mTOR) inhibitor, GDC-0980, that potentially could affect both O_2 supply and consumption was evaluated. The PI3K/mTOR pathway is a key signaling pathway in human cancer. The pathway not only plays an important role in tumor cell signaling, which affects O_2 consumption, but also is a key component of VEGF receptor 2 intracellular signaling in vascular endothelial cells, which can affect O_2 supply [17]. The potent and selective dual PI3K/mTOR inhibitor, GDC-0980, has been shown to produce a strong and rapid antivascular response in murine xenograft tumor models [17]. However, the effects of dual PI3K/mTOR inhibition on tumor oxygen level remain unknown. Given that GDC-0980 has entered clinical development [18], it will be valuable to ascertain the tumor metabolic changes associated with PI3K/mTOR inhibition.

Materials and Methods

PFC Emulsion Preparation

Perfluoro-15-crown-5-ether (SynQuest Laboratories, Inc, Alachua, FL) was mixed with an emulsifying solution of lecithin soy (MP Biomedicals, Solon, OH) and lactated Ringers solution (Baxter, Deerfield, IL). The mixture was processed using a microfluidizer (LV1; Microfluidics, Newton, MA) at 30,000 psi to form emulsions with a mean diameter of 250 nm, as measured by dynamic light scattering (DynaPro Nanostar; Wyatt Technology, Santa Barbara, CA). The final concentration of perfluoro-15-crown-5-ether was 60% wt/vol. The PFC solutions were then sterilized by microfiltration using membrane filters with a pore size of 0.45 μm (Thermo Scientific, Waltham, MA) and adjusted to a pH of 7.4.

Animal Preparation

The Institutional Animal Care and Use Committee at Genentech Inc (South San Francisco, CA) approved all animal protocols in this study. Female athymic nude mice (n = 50, 20-25 g; Harlan Laboratories, Indianapolis, IN) were inoculated subcutaneously on the hindlimb with HM-7 colorectal cancer cells (3.5×10^6 cells per mouse). The animals that were used in the study had an approximate tumor volume range of 150 to 250 mm^3 (volume = 0.5 × length × width^2) at the time when the animals entered the study. Animals were injected intravenously (i.v.) with 400 μl of the PFC solution at 48 hours and, again, at 24 hours before MRI.

Mice were placed under anesthesia by administration of 2% isoflurane in a warm anesthesia induction box and then placed in a custom-built animal holder and moved to the magnet bore, where anesthesia was maintained with 1% to 2% isoflurane that was adjusted according to the respiration rate of the animal. The animals' breathing rate was monitored, and temperature was maintained at 37°C using warm airflow controlled by a LabVIEW software module with feedback provided by a rectal temperature probe (SA Instruments, Stony Brook, NY).

MRI Measurements

Experiments were performed on a 9.4-T Agilent MRI System equipped with a ^{1}H/^{19}F 10-mm surface coil (Agilent Technologies Inc, Santa Clara, CA). ^{1}H-MRI measurements were performed first. Twelve 1-mm-thick coronal slices were acquired (field of view = 25.6 × 25.6 mm, matrix = 64 × 64). A diffusion-weighted fast spin-echo multislice (FSEMS) sequence was used to calculate an ADC spatial map with the following parameters: six b values ranging from 270 to 1000 s/mm^2, repetition time (TR) = 3 seconds, echo train length = 4, echo spacing = 3.95 milliseconds, number of averages (NA) = 2, diffusion gradient separation (Δ) = 30 milliseconds, duration (δ) = 3.3 milliseconds, resulting in a total scan time of 9 minutes. A spin echo multislice (SEMS) sequence was used to generate T_2 and M_0 maps that employed the following parameters: echo times = 5, 26, 47, and 68 milliseconds, TR = 3 seconds, NA = 1, and a scan time of 12 minutes. Spatial maps of ADC were obtained from the diffusion data by applying a linear least-squares regression to the natural logarithm of the signal intensity. Similarly, T_2 maps were obtained from the T_2-weighted, spin-echo data by a linear least-squares regression [12].

^{19}F-MRI was then carried out (field of view = 25.6 × 25.6 mm, matrix = 32 × 32, zero-filled to 64 × 64). A ^{19}F-weighted SEMS sequence was used to obtain a fluorine anatomic reference image (TR = 5 seconds, echo time = 8.5 milliseconds, NA = 4, scan time of 10 minutes). A ^{19}F single-shot, inversion recovery FSEMS sequence was employed to generate spatial maps of R_1 [FSEMS, inversion times (TI) = 0.1, 0.3, 0.5, 0.6, 0.7, 0.9, 1.2, 1.8, and 2.5 seconds; TR = 6 seconds, echo spacing = 4.1 milliseconds, echo train length = 32,

NA = 32, a scan time of 29 minutes]. Then, the R_1 of the ^{19}F nucleus was calculated by using the following equation [19]:

$$I(TI) = I_0 * \left(1 - a * e^{-R_1 * TI}\right), \quad (1)$$

where I(TI) is the signal intensity at time TI, I_0 is the signal intensity at equilibrium magnetization, a is a coefficient, and R_1 is the spin-lattice relaxation rate. R_1, a, and I_0 are determined from Equation 1 using a nonlinear regression algorithm. The pO_2 was then determined according to the calibration curve between R_1 and pO_2. The calibration curve was obtained by measuring the R_1 of PFC phantoms at known concentrations of dissolved oxygen (0%, 10%, 21%, 60%, and 100%). Twenty-one percent of oxygen corresponds to 160 mm Hg, and 100% of oxygen corresponds to 760 mm Hg. Phantoms were prepared in triplets.

MS Analysis

MS analysis of the ^1H data was used for tissue segmentation. K-means (KM) clustering was performed using the ADC, proton density, and T_2 maps as previously described [12,20,21]. The KM algorithm segmented the tumors into the following four tissue classes: viable tumor tissue, subcutaneous adipose tissue, low-T_2 necrotic class, and high-ADC necrotic class. The low-T_2 necrotic class represents an area of necrosis with active or recent hemorrhage, and the high-ADC necrotic class has been found to represent an acellular "cyst-like" region [12]. The tissue class map was combined with the ^{19}F pO_2 map to estimate pO_2 in the four tissue classes.

Histologic Analysis

After the final imaging time point, the animals were injected intraperitoneally (20 mg/kg) with hypoxyprobe (Hypoxyprobe Inc, Burlington, MA) 1 hour before being killed by cervical dislocation under anesthesia. The tumors were extracted and fixed in 10% neutral buffered formalin solution. Hematoxylin and eosin, MECA-32, and hypoxyprobe stains were used to identify tissue architecture, blood vessels, and hypoxic cells, respectively. The histologic hypoxic region was identified by hypoxyprobe staining that is typically considered to label cells present in a hypoxic environment where the pO_2 is between 0 and 10 mm Hg [22]. Histologic viable tumor tissue was identified by hematoxylin and eosin staining.

Whole slide images were acquired by the Olympus Nanozoomer automated slide scanning platform (Hamamatsu, Bridgewater, NJ) at ×200 final magnification. Scanned slides were analyzed in the Matlab software package (version R2011b by MathWorks, Natick, MA) as 24-bit RGB images. Various tumor regions (viable area, necrotic area, hypoxyprobe positive) were identified using a combination of support vector machines (SVMs) [23] and genetic programming [24]. A training set of representative areas was first generated manually and assigned a binary classification (positive for the region of interest or negative for regions to exclude). Then, an SVM was trained using RGB and texture values from these selections. Application of this SVM resulted in a binary image for each selection, and the noise in the resulting images was removed through the application of genetic programming, which found a sequence of simple morphologic operators that maximized the solution accuracy for both positive and negative selections, which was then applied to the entire image.

The analysis of vascular density was restricted to viable tumor tissue. A segmentation algorithm uses a sequence of morphologic operations to consolidate MECA-32–stained areas into individual vessels. The identification of vessels was aided by including vessel lumens, as characterized by empty white spaces that are adjacent to MECA-32–stained regions. Size and shape-based filtering of the resulting objects was used to remove noise. The vessel density here was defined as the vessel perimeter divided by the viable tumor area (mm^{-1}). Similarly, the percent hypoxic fraction was measured as the hypoxyprobe stain–positive area divided by the viable tumor area (%).

Experimental Protocols

Validation study. In the validation study, the first group of mice (n = 10) received two consecutive ^{19}F R_1 measurements acquired at normoxia (21% O_2) to assess the intrasessional reproducibility of the pO_2 measurement. For a second group of mice (n = 20), ^{19}F R_1 maps were acquired at normoxia (21% O_2) and during hyperoxia (carbogen: 95% O_2, 5% CO_2) conditions, which were done sequentially by changing the breathing gas. A 10-minute gap was employed between the two acquisitions to allow for the blood oxygenation to reach equilibrium, where the blood oxygen saturation was continuously monitored by the O2C System (LEA Medizintechnik GmbH Inc, Giessen, Germany) on the hind footpad of the animal. The MS estimates of the hypoxic region ($0 < pO_2 < 10$ mm Hg) in viable tumor tissue were compared with the histologic estimates of hypoxia (hypoxyprobe analysis).

Treatment studies. Treatment studies were performed in two additional cohorts of mice. In the first treatment study, B20.4.1.1 treatment (10 mg/kg, n = 13) or a control IgG (n = 11) was administrated as a single i.v. dose. Imaging was performed pretreatment (day 0) and 24 hours posttreatment (day 1). In the second study, B20.4.1.1 (10 mg/kg, n = 10) was administered as a single i.v. dose after pretreatment imaging on day 0. In the second group, GDC-0980 (10 mg/kg, n = 10) was administered orally daily on days 0, 1, and 2. For the control group (n = 10), a control IgG and 0.5% methycellulose/0.2% Tween 80 were used as controls for B20.4.1.1 and GDC-0980, respectively. Imaging was performed on day 0, 1, 2, and 3.

Statistical Analysis

Statistical significance was defined as $P < .05$. To compare two groups, an unpaired t test was used. To compare pretreatment to posttreatment data within a group, a paired t test was used. Statistical analysis was performed with JMP 9 (SAS Institute, Cary, NC) and Excel 2010 (Microsoft Inc, Redmond, WA). Data are presented as means ± standard error.

Results

Reproducibility of In Vivo *MS ^{19}F-MRI*

The uptake of the PFCs was significant but variable within the tumor (Figure 1, *A* and *B*). A very strong ^{19}F signal was visualized within some areas of the viable tissue class (Figure 1, *B* and *C*), consistent with the presence of vessels in these regions. In addition, strong ^{19}F uptake was observed in the low-T_2 necrosis class (Figure 1*B*, *green arrows*), where leakage is likely due to hemorrhage. This class has been found histologically to contain intact RBCs that shorten the T_2 and is likely an area of recent or active hemorrhage [12].

The ^{19}F R_1 maps of PFC calibration samples were obtained, and these data were then used to estimate pO_2 for all studies according to the measured linear relationship between R_1 and the oxygen level

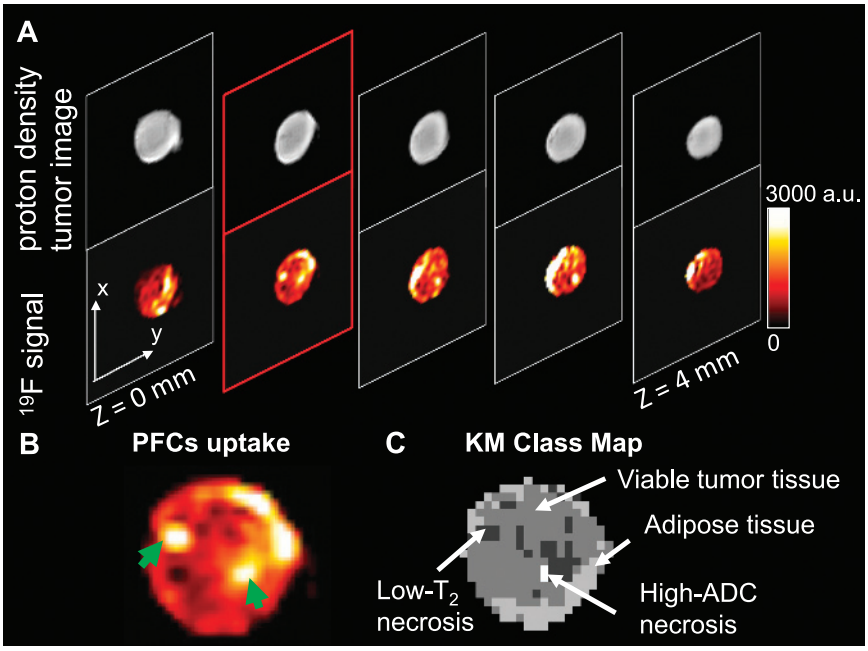

Figure 1. Anatomic images of PFC uptake in an HM-7 xenograft tumor. (A) The ^{19}F density images acquired in the same anatomic locations with ^{1}H density images reveal variable, albeit adequate PFC uptake. (B) A sample image of PFC uptake from the second slice in A is highlighted in red. The PFC uptake was heterogeneous. Some areas showed strong uptake of PFCs in the center of the tumor slice (green arrowheads). (C) The corresponding KM class map for the slice in B revealed that strong uptake of PFCs occurred in some areas of viable tumor, some areas of adipose tissue, and the low-T_2 necrosis class.

[R_1 = 0.0246 * O_2 (%) + 0.7473, R^2 = 0.999; Figure W1]. To test the intrasessional reproducibility of pO_2 measurements, two ^{19}F R_1 mapping acquisitions were made under normoxia (Figure 2*A*). The mean pO_2 values of the two acquisitions for each of the four classes are given as follows: viable tumor class, 51.92 ± 9.21 and 56.22 ± 9.24 mm Hg (P = .42); adipose tissue class, 55.16 ± 9.87 and 52.45 ± 9.71 mm Hg (P = .59); low-T_2 necrosis class, 53.26 ± 12.91 and 55.27 ± 15.07 mm Hg (P = .82); high-ADC necrosis class, 44.35 ± 17.23 and 33.42 ± 10.90 mm Hg (P = .84). The repetitive measurements revealed no significant change of mean pO_2 over time in all four tissue classes (P > .05, paired t test). The overall tumor response is a weighted average of all four tissue classes; therefore, the overall tumor did not exhibit a difference between the two measurements (49.98 ± 9.16 and 51.96 ± 9.53 mm Hg, P = .50; Figure 2*A*). An example of consecutive pO_2 estimates of the same tumor are shown in Figure 2*B*.

MS ^{19}F-MRI Detects pO_2 Increase in Viable Tumor due to Carbogen Challenge

To test the hypothesis on tumor heterogeneity and pO_2 response, a second group of mice underwent a carbogen breathing gas challenge. Two measurements were made under normoxia and hyperoxia, respectively. Under the breathing gas challenge, there was a heterogeneous response within the tumor (Figure 3). Statistical analysis revealed that the viable tumor class (normoxia: 45.73 ± 4.30 mm Hg; hyperoxia: 61.06 ± 5.98 mm Hg, paired t test, P = .018), adipose tissue class (normoxia: 54.80 ± 5.75 mm Hg; hyperoxia: 65.71 ± 7.13 mm Hg, P < .01), and low-T_2 necrosis class (normoxia: 32.46 ± 5.98 mm Hg; hyperoxia: 44.64 ± 8.02 mm Hg, P < .01) exhibited a significant increase in pO_2 in response to hyperoxia challenge (Figure 3*A*), where both viable regions (viable tumor and adipose tissue) showed an increase in pO_2 consistent with a vascularized tissue. The increase in pO_2 for the low-T_2 necrosis class provided further evidence of active hemorrhage. The high-ADC necrosis class showed no significant change in pO_2 (normoxia: 34.37 ± 5.09 mm Hg; hyperoxia: 43.44 ± 8.67 mm Hg, P = .10), consistent with the acellular "cyst-like" nature of the region [12]. An example of the response of a tumor to the breathing gas challenge is shown in Figure 3*B*.

MS ^{19}F-MRI In Vivo *Estimate of Hypoxic Area Correlates with Histologic Staining of Hypoxic Cells*

The *in vivo* estimate of hypoxic area by MS ^{19}F-MRI exhibited a strong correlation (r = 0.79, P < .01) with the *ex vivo* estimate of hypoxia derived from the hypoxyprobe stain–positive area histologic analysis (Figure 4*A*). The MRI hypoxia region was defined as pO_2 values between 0 and 10 mm Hg based on the *in vivo* pO_2 maps (Figure 4*B*, *red*). Histologically hypoxic (hypoxyprobe-positive) tissue (Figure 4*B*, *brown*) corresponds to areas in which the cellular pO_2 is below 10 mm Hg. The histologic hypoxic area in viable tissue was assessed in a centrally located section of each tumor (approximately coplanar with the MRI plane) and was then compared with the corresponding imaging slice in the *in vivo* MRI data.

MS ^{19}F-MRI Detects Decrease of pO_2 after Anti-VEGF (B20.4.1.1) Treatment

In the first treatment study, the B20.4.1.1-treated group ($\Delta_{day\ 1\ -\ day\ 0}$ = 7.38 ± 7.53 mm^3) at 24 hours posttreatment did not exhibit a significant difference in viable tumor growth, identified by MS classification, when compared with control ($\Delta_{day\ 1\ -\ day\ 0}$ = 19.07 ± 6.17 mm^3, P > .05; Figure 5*A*). However, a significant reduction in pO_2 was detected

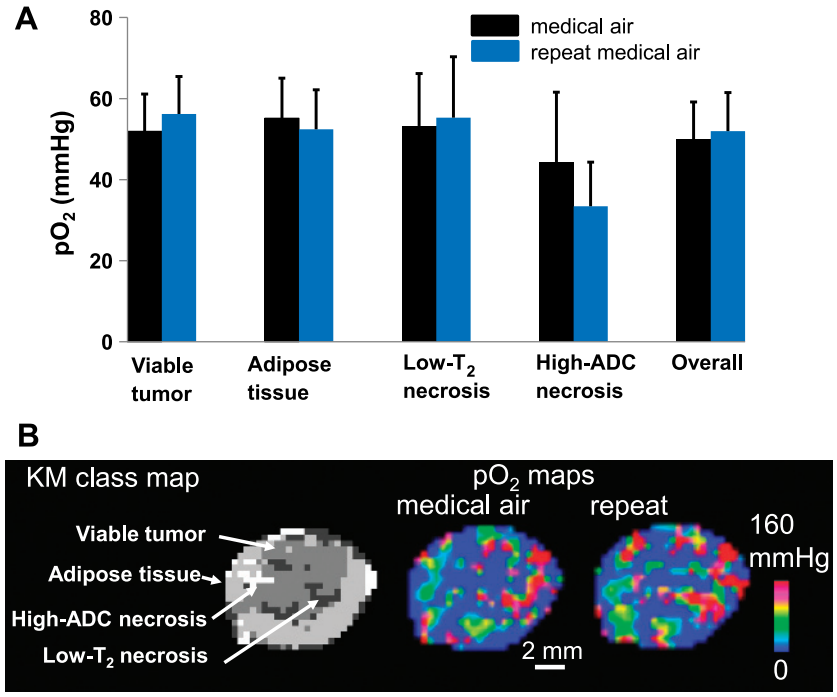

Figure 2. Repeated pO_2 measurements revealed no significant change over time in the HM-7 mouse xenograft tumor model. (A) Two consecutive pO_2 data sets were obtained under normoxia (black and blue). There was no significant change of mean pO_2 over time in all four tissue classes. The overall tumor response is a weighted average of all four tissue classes. Data are shown as means ± SEM. (B) An example of a pO_2 spatial map for the same tumor slice generated from the two consecutive measurements.

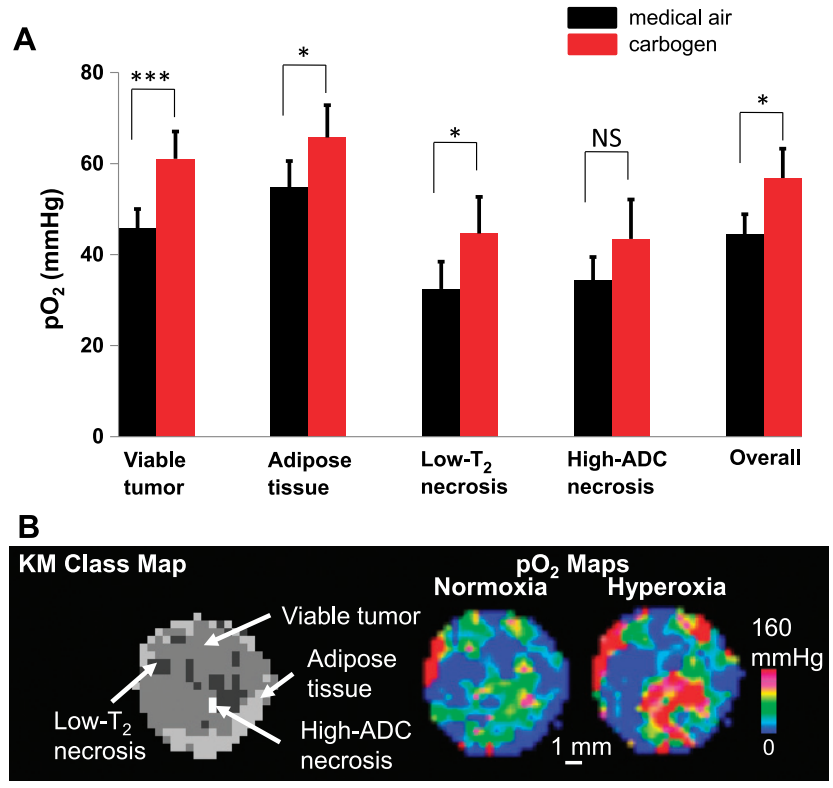

Figure 3. The change in mean pO_2 under hyperoxia challenge for the MS tissue classes. (A) pO_2 data were acquired under normoxia (black) and once again under carbogen (95% O_2, 5% CO_2) breathing gas challenge (red). The pO_2 in viable tumor class increased from 45.73 ± 4.30 to 61.06 ± 5.98 mm Hg, and the adipose tissue class and low-T_2 necrosis class also exhibited a significant increase of pO_2. The high-ADC necrosis class showed no change in pO_2. The overall response is a weighted average of the four tissue classes. Data are shown as means ± SEM. (B) An example of a pO2 spatial map response to hyperoxia challenge. There was a heterogeneous response within the tumor, some areas increased dramatically, whereas other regions did not respond. *$P < .05$ and ***$P < .001$; NS, not significant.

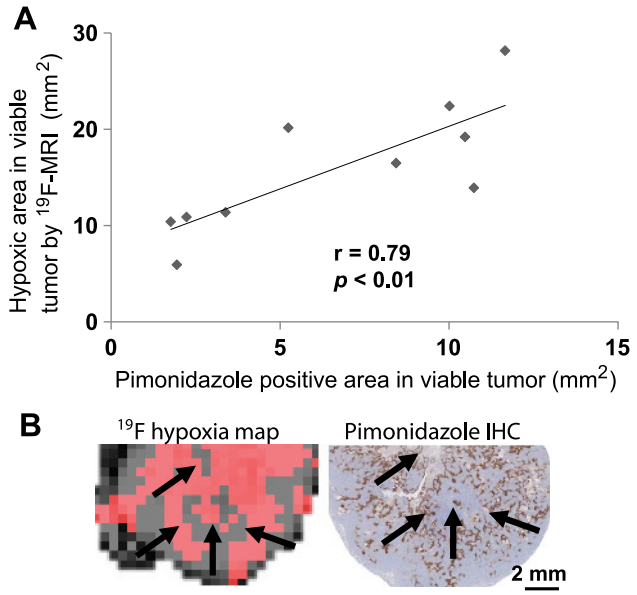

Figure 4. MS ^{19}F-MRI–identified hypoxic regions in viable tumor correlate with histology. (A) A one-to-one comparison between the hypoxic area in viable tissue for the center slice of each tumor measured by MS ^{19}F-MRI and pimonidazole-positive area in viable tissue in the corresponding tumor slice measured by histology showed a significant correlation. (B) The MRI hypoxia region was shown in red, and the histologic hypoxia area was shown in brown. The images showed similar patterns of hypoxia (pointed by arrows).

within the viable tumor. The B20.4.1.1-treated group showed a reduction of viable tumor pO_2 not only with respect to its pretreatment level ($\Delta_{day\ 1\ -\ day\ 0}$ = −18.78 ± 3.92 mm Hg, $P < .001$) but also in comparison with the control group ($\Delta_{day\ 1\ -\ day\ 0}$ = −4.27 ± 5.52 mm Hg, $P < .05$; Figure 5*B*), which can also be visually confirmed in the representative images (Figure 5*C*).

Histology Confirms MS ^{19}F-MRI Assessment of an Anti–VEGF-Induced Hypoxic Response

The reduction of pO_2 in viable tumor in the B20.4.1.1 group was attributed to the reduction of vessel density that was quantified by MECA-32 staining (Figure 6*A*). Compared with the control group (7.96 ± 0.76 mm^{-1}), the B20.4.1.1-treated group exhibited a 40% decrease in vessel density (4.76 ± 0.40 mm^{-1}, $P < .01$; Figure 6*B*). Consistent with the MRI pO_2 results, tissue hypoxia measured by hypoxyprobe staining showed that at 24 hours posttreatment, the B20.4.1.1-treated group exhibited an increased hypoxic area fraction (Figure 6*C*) of approximately 13% [B20.4.1.1 (30.14 ± 2.78%) *vs* control (17.11 ± 4.00%), $P < .02$; Figure 6*D*].

Dual PI3K/mTOR Inhibition Induces a Sustained Hypoxic Response in Viable Tumor

In the second treatment study, PFCs remained in the tumor throughout the course of the 4-day study following i.v. injection. No significant loss of ^{19}F signal was observed during the 4-day period (Figure 7*A*), which enabled the longitudinal study of pO_2 changes over this time period. In general, both the B20.4.1.1- and GDC-0980–treated groups showed decreased pO_2 in viable tumor, relative to pretreatment levels, following the onset of treatment. In the B20.4.1.1-treated group, the pO_2 values in viable tumor on day 1 ($\Delta_{day\ 1\ -\ day\ 0}$ = −13.26 ± 5.02 mm Hg), day 2 ($\Delta_{day\ 2\ -\ day\ 0}$ = −10.31 ± 3.06 mm Hg), and day 3 ($\Delta_{day\ 3\ -\ day\ 0}$ = −12.67 ± 6.35 mm Hg) were all significantly lower than baseline at day 0 ($P < .05$). When compared with the control group on day 1 ($\Delta_{day\ 1\ -\ day\ 0}$ = −2.15 ± 5.12 mm Hg), day 2 ($\Delta_{day\ 2\ -\ day\ 0}$ = −3.55 ± 5.75 mm Hg), and day 3 ($\Delta_{day\ 3\ -\ day\ 0}$ = −2.26 ± 5.33 mm Hg), the changes in pO_2 for the B20.4.1.1-treated group did not differ significantly from the changes observed for the control group on any of the 3 days (P values were .14, .33, and .24 for days 1, 2, and 3, respectively; Figure 7*B*). GDC-0980 had a strong effect for all 3 days after the onset of the treatment relative to its baseline at day 0

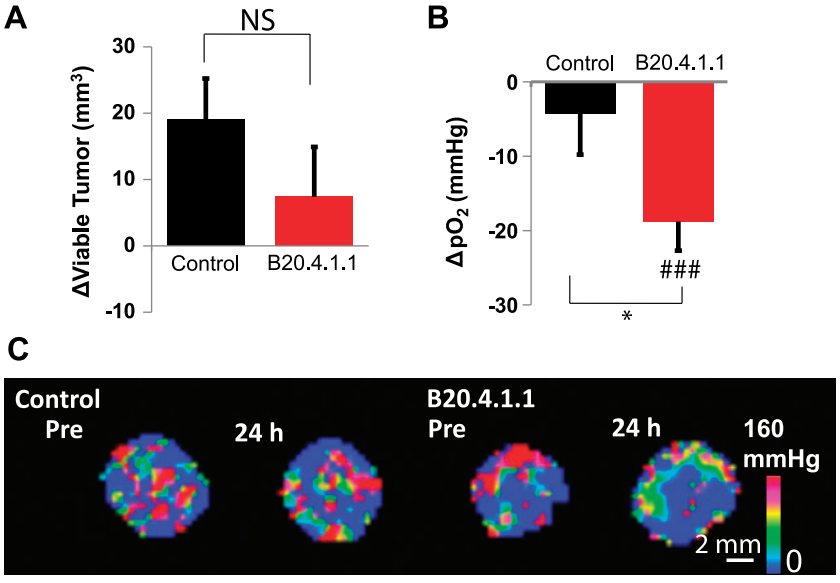

Figure 5. At 24 hours posttreatment, B20.4.1.1 exhibited a significant decrease in viable tumor pO_2. (A) The B20.4.1.1-treated group showed no significant change in viable tumor volume (NS, $P > .05$). (B) The viable tumor pO_2 was significantly reduced in the B20.4.1.1 group relative to the pretreatment level ($^{###}P < .001$) as well as in comparison with the control group ($^{*}P < .05$). (C) Images showing pO_2 change after 24 hours.

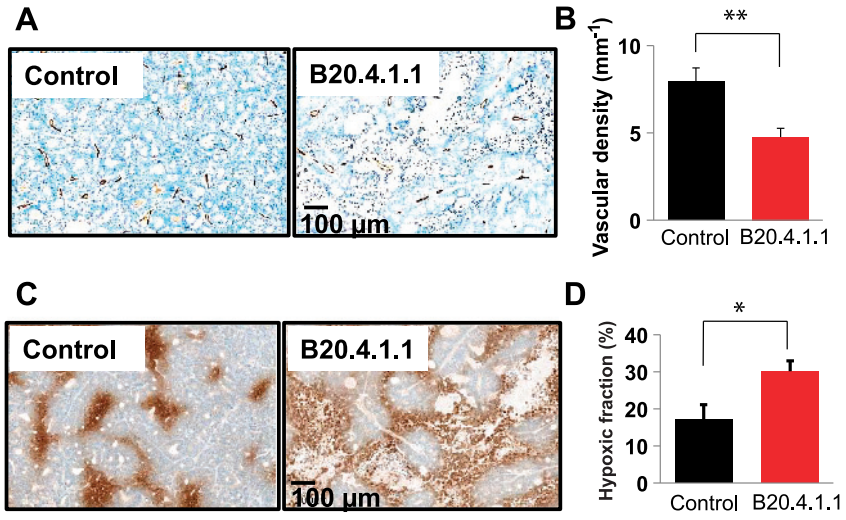

Figure 6. At 24 hours posttreatment, B20.4.1.1 significantly decreased vascular density and increased hypoxic fraction in the viable tumor. (A) Images show vessel density (brown, MECA-32 staining) at 24 hours posttreatment. Bar, 100 μm. (B) The B20.4.1.1 group showed a 40% reduction of vascular density in comparison with the control (**$P < .01$). (C) Images depict hypoxic cells (brown, hypoxyprobe staining) at 24 hours posttreatment. Bar, 100 μm. (D) The B20.4.1.1 group showed a 13% increase in the hypoxic fraction in comparison with the control (*$P < .02$).

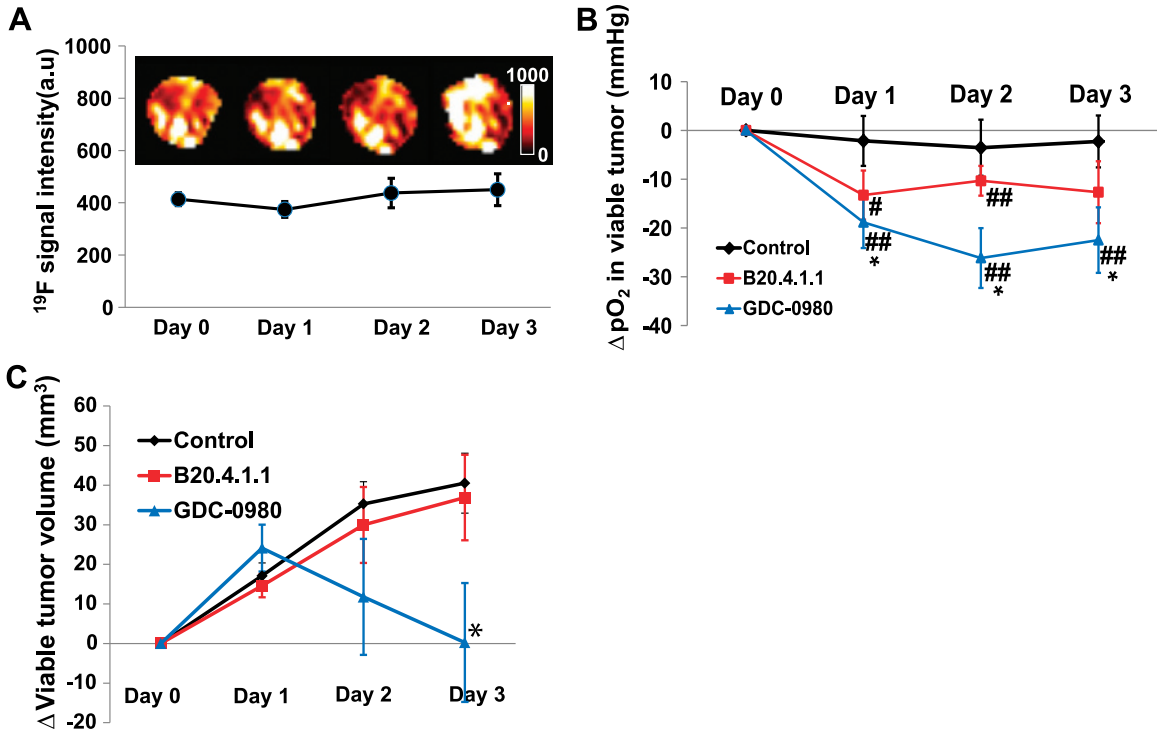

Figure 7. (A) PFCs remained in the tumor throughout the course of the 4-day study following i.v. delivery. No significant loss of ^{19}F signal was observed, which enabled a multiday longitudinal study of pO_2 change. Every effort was made to locate the same imaging slice in the tumor according to the distance and shape, but deviations may still exist due to the positioning of the animal on different days, as well as tumor growth. (B) The temporal evaluation of mean ΔpO_2 in viable tumor. Both the B20.4.1.1 and GDC-0980 groups exhibited a decrease in pO_2 in the viable tumor posttreatment relative to pretreatment levels. When compared with the control group, the GDC-0980 group exhibited a significant decrease in viable tumor pO_2, whereas the B20.4.1.1 group showed a trend toward a reduction of pO_2 ($P = .14$ on day 1). (C) The viable tumor volume change with time. Only the GDC-0980 group showed a significant reduction on day 3 in comparison with the control. *$P < .05$ in comparison with the control group. $^{\#}P < .05$ *versus* pretreatment; $^{\#\#}P < .01$ *versus* pretreatment. Data are shown as means ± SEM.

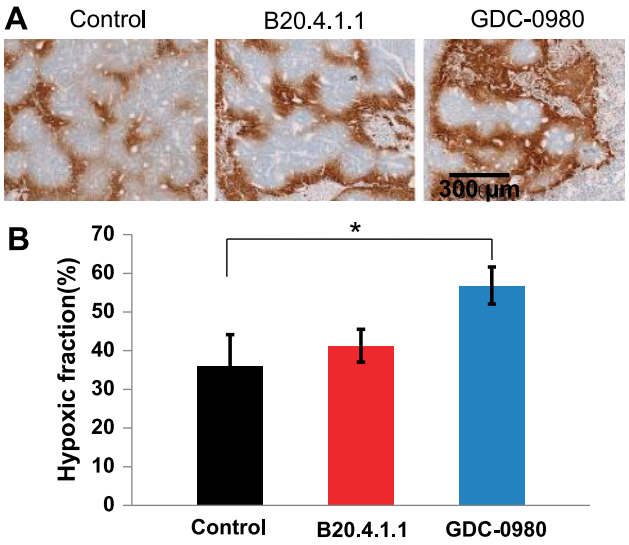

Figure 8. At 72 hours posttreatment, GDC-0980 significantly increased the hypoxic fraction in viable tumor as assessed by histology. (A) Images showed hypoxic cells at 72 hours posttreatment. Bar, 300 μm. (B) GDC-0980 showed a significant increase in hypoxic fraction (*$P < .05$), whereas the B20.4.1.1-treated group showed no significant change ($P > .05$).

($\Delta_{day\ 1\ -\ day\ 0}$ = −18.85 ± 5.24 mm Hg, $P < .01$; $\Delta_{day\ 2\ -\ day\ 0}$ = −26.16 ± 6.12 mm Hg, $P < .01$; $\Delta_{day\ 2\ -\ day\ 0}$ = −22.49 ± 6.72 mm Hg, $P < .01$; Figure 7*B*). When compared with the control group, the GDC-0980 group exhibited a significant decrease in viable tumor pO_2 ($P < .05$). The significant decrease of pO_2 in the GDC-0980 treatment group occurred only in the viable tumor, whereas there were no significant pO_2 changes detected relative to control in any of the other tissue classes (Figure W2). Similar to the first study, the B20.4.1.1-treated group ($\Delta_{day\ 1\ -\ day\ 0}$ = 14.61 ± 2.94 mm^3, $P > .05$; $\Delta_{day\ 2\ -\ day\ 0}$ = 29.96 ± 9.58 mm^3, $P > .05$; $\Delta_{day\ 3\ -\ day\ 0}$ = 36.86 ± 10.80 mm^3, $P > .05$) did not exhibit a significant difference in viable tumor growth when compared with control ($\Delta_{day\ 1\ -\ day\ 0}$ = 17.09 ± 3.25 mm^3, $\Delta_{day\ 2\ -\ day\ 0}$ = 35.26 ± 5.60 mm^3, and $\Delta_{day\ 3\ -\ day\ 0}$ = 40.52 ± 7.58 mm^3). Only the GDC-0980 group showed a significant reduction on day 3 in comparison with the control group ($\Delta_{day\ 1\ -\ day\ 0}$ = 24.11 ± 5.90 mm^3, $P > .05$; $\Delta_{day\ 2\ -\ day\ 0}$ = 11.78 ± 14.64 mm^3, $P > .05$; $\Delta_{day\ 3\ -\ day\ 0}$ = 0.26 ± 15.00 mm^3, $P < .05$; Figure 7*C*).

MS ^{19}F-MRI Predicted Histologic Findings for Both GDC-0980 and B20.4.1.1

The MRI pO_2 results were further confirmed by histology (Figure 8*A*). Compared with the control group, the GDC-0980–treated group exhibited a 20% increase in hypoxic fraction ($P < .05$), whereas the B20.4.1.1-treated group showed no significant change in comparison with control (Figure 8*B*). The histologic staining further revealed no significant change of vessel density between the B20.4.1.1-treated group and the control group ($P = .60$), whereas a trend toward reduction of vessel density in the GDC-0980-treated group ($P = .066$) was observed (data not shown).

Discussion

This is the first study to employ a diffusion-based MS tissue segmentation approach to address the complications of tissue heterogeneity in ^{19}F-MRI pO_2 mapping. The validation study demonstrated that this approach can detect tissue-dependent oxygenation changes in response to a breathing gas challenge, and this *in vivo* technique showed a good correlation with histologic estimates of hypoxia. The results from the treatment studies to assess the effects of two antivascular agents on tumor oxygenation demonstrated a rapid reduction in viable tumor pO_2 after treatment. Dual PI3K/mTOR inhibition by GDC-0980 strongly suppresses tumor oxygenation consistent with the known antivascular response for this molecule [17]. Anti-VEGF treatment significantly lowered viable tumor pO_2 relative to control in the first study but did not achieve statistical significance in the second study. In both treatment studies, *in vivo* MS ^{19}F-MRI pO_2 estimates predicted the histologic hypoxia results. These results advocate for the use of this MS ^{19}F-MRI technique as a tool to better understand the mode of action of therapies that alter the tumor's microenvironment.

Different PFCs have been used for *in vivo* oxygenation studies [10]. The perfluoro-15-crown-5-ether employed in this study as an imaging contrast agent has two major advantages over other PFCs: its sensitivity for measuring small changes in pO_2 [4] and a lack of tissue toxicity [25]. The R_1 parameter for the PFC contrast agent was measured to obtain pO_2 estimates. Consistent with previously publish studies, the R_1 relaxation rate of perfluoro-15-crown-5-ether is a linear function of oxygen level (R^2 = 0.999) at 37°C at 9.4 T [4,7,25]. While the pO_2 measured in the current study is similar to some previous studies [4,7], differences do exist with pO_2 values measured under different settings in other studies [26,27]. These differences may be due to the fact that pO_2 values have been shown to vary with tumor cell line, tumor size, and tissue heterogeneity [27,28], as well as the methodology that was used for measurements [6]. In addition, the method of PFC administration may affect the relative spatial PFC distribution. Although i.v. injection gives a more global measurement when compared with local PFC injection directly into the tumor, i.v. delivery of PFCs may bias pO_2 estimates toward well-perfused areas and regions close to the blood vessels [29]. In the current studies, PFCs were administrated before treatments, when the tumors were highly vascularized, and this resulted in the PFCs being delivered and retained in the tumor at a sufficient level to make reliable pO_2 measurements throughout the study. Thus, any induced hypoxia due to treatment or tumor growth that occurs after PFCs were administrated could be accurately measured because the PFCs are already present in the tumor.

In this study, tumor heterogeneity is addressed by employing diffusion-based MS analysis to differentiate distinct tissue classes. A reproducibility study was performed by assessing the consistency of the pO_2 estimates for the four tissue classes from two repetitive measurements made under normoxic conditions. The class estimates were found not to differ significantly, demonstrating the reproducibility of the technique. It is worth noting that although there is no statistical difference between the two measurements, the two pO_2 maps were not fully identical on a voxel-by-voxel basis. These apparent voxel differences could be due to local acute hypoxic fluctuations that have been observed in tumors [30,31]. The current method, however, cannot fully resolve these transient changes in pO_2 due to its low temporal resolution. Apart from these physiological factors, the system and measurement noise could also contribute to specific voxel differences.

Different tissue responses were observed during the hyperoxia challenge experiment, which provides further support for this MS approach. The viable tumor and subcutaneous adipose tissue are well-vascularized tissues and, thus, respond actively to the hyperoxia challenge. The low-T_2 necrosis class exhibited an increase in pO_2 on

breathing gas challenge. This could be due to several possible mechanisms that include the following: Circulating RBCs with an increased oxygen load may have entered the region due to active hemorrhage. Another possibility is that there may have been an increase in oxygen diffusing from the neighboring viable tissue. In addition, partial volume contamination from neighboring viable tissue may have contributed to the response. The high-ADC necrosis class did not show a significant change in pO_2, which is consistent with its acellular cyst-like nature [12], although the presence of an apparent trend in the data may be due to partial volume influence from neighboring viable tissue. The differing sensitivity in response to the gas challenge among the four tissue classes is likely due to the difference in pathophysiological features of these tissue classes that have been previously characterized [12,20,21]. These results indicate that the inclusion of nonviable tumor tissue regions in whole-tumor estimates of pO_2 response can mask or bias the changes of pO_2 within the tissue of therapeutic interest (viable tumor) depending on the relative volume ratio of each tissue class. Restricting the analysis of tumor oxygenation to the viable tumor is physiologically meaningful and could aid investigations of therapeutic responses.

The MS ^{19}F-MRI approach to assessing pO_2 within viable tumor was applied to serially monitor the effects of antivascular therapies on tumor oxygenation. Two treatments were used in this study, an anti-VEGF molecule (B20.4.1.1) and a dual PI3K/mTOR inhibitor (GDC-0980). The effect of antivascular agents on tumor oxygenation has been in question for a number of years. Some studies have shown increased tumor hypoxia after anti-VEGF treatment [13,15,16], whereas other studies show decreased tumor hypoxia (increased pO_2) [14,32,33]. These different observations may be explained in part by the role of vessel normalization in the response of tumors to antiangiogenic therapy where antiangiogenic therapies initially improve both the structure and the function of tumor vessels, whereas sustained or more aggressive antiangiogenic regimens eventually prune away functional vessels resulting in a more hypoxic environment [34]. In the current studies, anti-VEGF (B20.4.1.1) treatment did not cause an increase in viable tumor pO_2. This may be due to the strong antivascular response caused by a 10 mg/kg dose of B20.4.1.1, resulting in a very short or the complete absence of a transient normalization window occurring after treatment. These results are consistent with previous findings where B20.4.1.1 was shown to reduce vascular density and inhibit tumor growth [17,35]. Although no evidence of an increase of pO_2 was observed in the current studies, the possibility of a pO_2 increase at earlier time points cannot be ruled out. The difference in pO_2 response by B20.4.1.1 treatment between the two treatment studies was likely due to the lack of statistical power. However, in both studies, the *in vivo* MRI pO_2 measurements predicted the *ex vivo* histologic results of hypoxic fraction for B20.4.1.1 treatment response relative to control. The other treatment that was evaluated, GDC-0980, a novel dual inhibitor of mTOR and PI3K, exhibited a significant decrease in viable tumor pO_2 ($P < .05$). *Ex vivo* histologic measurements of hypoxic fraction confirmed a significant increase in hypoxic fraction of the GDC-0980–treated tumors. The strong suppression of pO_2 induced by GDC-0980 is likely because of the suppression of oxygen supply due to the loss of small functional vessels as previously demonstrated [17]. In addition, compared to B20.4.1.1, an anti–VEGF-A monotherapy, GDC-0980 treatment resulted in greater tumor growth inhibition due to both PI3K pathway inhibition in the tumor cells and a strong antivascular effect [17]. It is also important to note that among the four tissue classes, viable tumor was the only class where GDC-0980 produced a statistically significant decrease in pO_2 relative to the changes observed in the control group (Figure W2). This supports the notion that, depending on the relative volume ratio of each tissue class, the inclusion of nonviable tumor tissue regions in whole-tumor estimates of pO_2 response can mask or bias the changes of pO_2 within the tissue of therapeutic interest (viable tumor). Furthermore, targeting hypoxia in tumors has been a great interest to the field of combination therapies [2,11,36]. In this sense, MS ^{19}F-MRI may provide a valuable tool for research efforts into combination therapies that target the altered microenvironment.

In conclusion, this work has demonstrated for the first time that pO_2 measurements can be restricted to the viable tumor and that the necrotic tissue classes contribute erroneous data to whole-tumor estimates of the pO_2 response. The MS ^{19}F-MRI approach provides a means to measure pO_2 within the viable tumor and address the issue of tumor heterogeneity that complicates pO_2 tumor imaging. In addition, this methodology has been employed to better understand the effects of antivascular agents on tumor oxygenation. Detected by MS ^{19}F-MRI, a potent and selective PI3K/mTOR inhibitor showed strong suppression of tumor oxygenation for the first time. These results advocate for the use of the MS ^{19}F-MRI technique as a tool to better understand the mode of action of therapies that alter the tumor's microenvironment and may provide insight into combination therapies that target the altered microenvironment.

Acknowledgments

The authors thank the *in vivo* cell culture team and laboratory animal resources at Genentech for their support in the imaging studies and Richard Vandlen, James Ernst, Michelle W. Lee, Mike Elliott, Jane Gunson, and Pradeep Nair for their assistance with PFC synthesis.

References

[1] Horsman MR, Mortensen LS, Petersen JB, Busk M, and Overgaard J (2012). Imaging hypoxia to improve radiotherapy outcome. *Nat Rev Clin Oncol* **9**, 674–687.

[2] Wilson WR and Hay MP (2011). Targeting hypoxia in cancer therapy. *Nat Rev Cancer* **11**, 393–410.

[3] Mason RP, Zhao D, Pacheco-Torres J, Cui W, Kodibagkar VD, Gulaka PK, Hao G, Thorpe P, Hahn EV, and Peschke P (2010). Multimodality imaging of hypoxia in preclinical settings. *Q J Nucl Med Mol Imaging* **54**, 259–280.

[4] Dardzinski BJ and Sotak CH (1994). Rapid tissue oxygen tension mapping using ^{19}F inversion-recovery echo-planar imaging of perfluoro-15-crown-5-ether. *Magn Reson Med* **32**, 88–97.

[5] Hunjan S, Zhao DW, Constantinescu A, Hahn EW, Antich PP, and Mason RP (2001). Tumor oximetry: demonstration of an enhanced dynamic mapping procedure using fluorine-19 echo planar magnetic resonance imaging in the Dunning prostate R3327-AT1 rat tumor. *Int J Radiat Oncol Biol Phys* **49**, 1097–1108.

[6] Jordan BF, Cron GO, and Gallez B (2009). Rapid monitoring of oxygenation by ^{19}F magnetic resonance imaging: simultaneous comparison with fluorescence quenching. *Magn Reson Med* **61**, 634–638.

[7] Kadayakkara DKK, Janjic JM, Pusateri LK, Young W-B, and Ahrens ET (2010). *In vivo* observation of intracellular oximetry in perfluorocarbon-labeled glioma cells and chemotherapeutic response in the CNS using fluorine-19 MRI. *Magn Reson Med* **64**, 1252–1259.

[8] Kodibagkar VD, Cui W, Merritt ME, and Mason RP (2006). Novel ^{1}H NMR approach to quantitative tissue oximetry using hexamethyldisiloxane. *Magn Reson Med* **55**, 743–748.

[9] Jordan BF, Magat J, Colliez F, Ozel E, Fruytier A-C, Marchand V, Mignion L, Bouzin C, Cani PD, Vandeputte C, et al. (2013). Mapping of oxygen by imaging lipids relaxation enhancement: a potential sensitive endogenous MRI contrast to map variations in tissue oxygenation. *Magn Reson Med* **70**, 732–744.

[10] Yu JX, Kodibagkar VD, Cui WN, and Mason RP (2005). 19F: a versatile reporter for non-invasive physiology and pharmacology using magnetic resonance. *Curr Med Chem* **12**, 819–848.

[11] Rapisarda A and Melillo G (2012). Overcoming disappointing results with antiangiogenic therapy by targeting hypoxia. *Nat Rev Clin Oncol* **9**, 378–390.

[12] Carano RAD, Ross AL, Ross J, Williams SP, Koeppen H, Schwall RH, and Van Bruggen N (2004). Quantification of tumor tissue populations by multispectral analysis. *Magn Reson Med* **51**, 542–551.

[13] Conley SJ, Gheordunescu E, Kakarala P, Newman B, Korkaya H, Heath AN, Clouthier SG, and Wicha MS (2012). Antiangiogenic agents increase breast cancer stem cells via the generation of tumor hypoxia. *Proc Natl Acad Sci USA* **109**, 2784–2789.

[14] Lee CG, Heijn M, di Tomaso E, Griffon-Etienne G, Ancukiewicz M, Koike C, Park KR, Ferrara N, Jain RK, Suit HD, et al. (2000). Anti-vascular endothelial growth factor treatment augments tumor radiation response under normoxic or hypoxic conditions. *Cancer Res* **60**, 5565–5570.

[15] Mehta S, Hughes NP, Buffa FM, Li SP, Adams RF, Adwani A, Taylor NJ, Levitt NC, Padhani AR, Makris A, et al. (2011). Assessing early therapeutic response to bevacizumab in primary breast cancer using magnetic resonance imaging and gene expression profiles. *J Natl Cancer Inst Monogr* **43**, 71–74.

[16] Rapisarda A, Hollingshead M, Uranchimeg B, Bonomi CA, Borgel SD, Carter JP, Gehrs B, Raffeld M, Kinders RJ, Parchment R, et al. (2009). Increased antitumor activity of bevacizumab in combination with hypoxia inducible factor-1 inhibition. *Mol Cancer Ther* **8**, 1867–1877.

[17] Sampath D, Oeh JR, Wyatt SK, Cao TC, Koeppen H, Eastham-Anderson J, Robillard L, Ho CC, Ross J, Zhuang G, et al. (2013). Multimodal microvascular imaging reveals that selective inhibition of class I PI3K is sufficient to induce an antivascular response. *Neoplasia* **15**, 694–711.

[18] Genentech (2009). *A Study Evaluating GDC-0980 Administered Once Weekly in Patients with Refractory Solid Tumors or Non-Hodgkin's Lymphoma. NCT00854126.*. The United States National Institutes of Health, available at http://clinicaltrials.gov/.

[19] Fan XB, River JN, Muresan AS, Popescu C, Zamora M, Culp RM, and Karczmar GS (2006). MRI of perfluorocarbon emulsion kinetics in rodent mammary tumours. *Phys Med Biol* **51**, 211–220.

[20] Berry LR, Barck KH, Go MA, Ross J, Wu X, Williams SP, Gogineni A, Cole MJ, Van Bruggen N, Fuh G, et al. (2008). Quantification of viable tumor microvascular characteristics by multispectral analysis. *Magn Reson Med* **60**, 64–72.

[21] Ungersma SE, Pacheco G, Ho C, Yee SF, Ross J, van Bruggen N, Peale FV Jr, Ross S, and Carano RAD (2010). Vessel imaging with viable tumor analysis for quantification of tumor angiogenesis. *Magn Reson Med* **63**, 1637–1647.

[22] Gross MW, Karbach U, Groebe K, Franko AJ, and Muellerklieser W (1995). Calibration of misonidazole labeling by simultaneous measurement of oxygen tension and labeling density in multicellular spheroids. *Int J Cancer* **61**, 567–573.

[23] Wang X, Wang T, and Bu J (2011). Color image segmentation using pixel wise support vector machine classification. *Pattern Recogn* **44**, 777–787.

[24] Hernandez MIQ (2004). Genetic Programming applied to Morphological Image Processing. PhD thesis, School of Computer Science, University of Birmingham.

[25] Mignion L, Magat J, Schakman O, Marbaix E, Gallez B, and Jordan BF (2013). Hexafluorobenzene in comparison with perfluoro-15-crown-5-ether for repeated monitoring of oxygenation using ^{19}F MRI in a mouse model. *Magn Reson Med* **69**, 248–254.

[26] Zhao D, Ran S, Constantinescu A, Hahn EW, and Mason RP (2003). Tumor oxygen dynamics: correlation of *in vivo* MRI with histological findings. *Neoplasia* **5**, 308–318.

[27] Zhao DW, Constantinescu A, Hahn EW, and Mason RP (2002). Differential oxygen dynamics in two diverse Dunning prostate R3327 rat tumor sublines (MAT-Lu and HI) with respect to growth and respiratory challenge. *Int J Radiat Oncol Biol Phys* **53**, 744–756.

[28] Mason RP, Hunjan S, Le D, Constantinescu A, Barker BR, Wong PS, Peschke P, Hahn EW, and Antich PP (1998). Regional tumor oxygen tension: fluorine echo planar imaging of hexafluorobenzene reveals heterogeneity of dynamics. *Int J Radiat Oncol Biol Phys* **42**, 747–750.

[29] Van der Sanden BPJ, Heerschap A, Simonetti AW, Rijken PFJW, Peters HPW, Stuben G, and van der Kogel AJ (1999). Characterization and validation of noninvasive oxygen tension measurements in human glioma xenografts by ^{19}F-MR relaxometry. *Int J Radiat Oncol Biol Phys* **44**, 649–658.

[30] Magat J, Jordan BF, Cron GO, and Gallez B (2010). Noninvasive mapping of spontaneous fluctuations in tumor oxygenation using ^{19}F MRI. *Med Phys* **37**, 5434–5441.

[31] Baudelet C, Ansiaux R, Jordan BF, Havaux X, Macq B, and Gallez B (2004). Physiological noise in murine solid tumours using T2*-weighted gradient-echo imaging: a marker of tumour acute hypoxia? *Phys Med Biol* **49**, 3389–3411.

[32] Dings RPM, Loren M, Heun H, McNiel E, Griffioen AW, Mayo KH, and Griffin RJ (2007). Scheduling of radiation with angiogenesis inhibitors anginex and avastin improves therapeutic outcome via vessel normalization. *Clin Cancer Res* **13**, 3395–3402.

[33] Myers AL, Williams RF, Ng CY, Hartwich JE, and Davidoff AM (2011). Bevacizumab-induced tumor vessel remodeling in rhabdomyosarcoma xenografts increases the effectiveness of adjuvant ionizing radiation. *J Pediatr Surg* **45**, 1080–1085.

[34] Jain RK (2005). Normalization of tumor vasculature: an emerging concept in antiangiogenic therapy. *Science* **307**, 58–62.

[35] Liang WC, Wu XM, Peale FV, Lee CV, Meng G, Gutierrez J, Fu L, Malik AK, Gerber HP, Ferrara N, et al. (2006). Cross-species vascular endothelial growth factor (VEGF)-blocking antibodies completely inhibit the growth of human tumor xenografts and measure the contribution of stromal VEGF. *J Biol Chem* **281**, 951–961.

[36] Jiang L, Greenwood TR, Artemov D, Raman V, Winnard PT Jr, Heeren RMA, Bhujwalla ZM, and Glunde K (2012). Localized hypoxia results in spatially heterogeneous metabolic signatures in breast tumor models. *Neoplasia* **14**, 732–741.

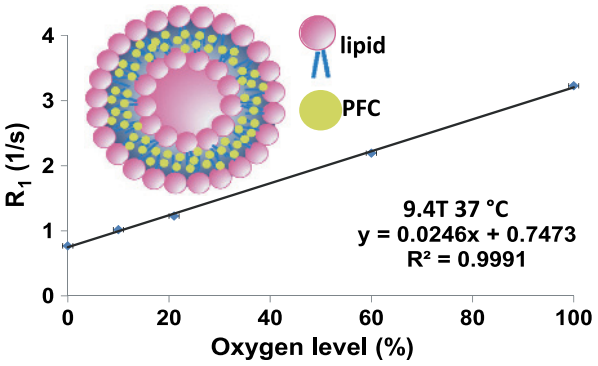

Figure W1. The linear relationship between the R_1 of perfluoro-15-crown-5-ether and the oxygen level. The cartoon depicts the structure of the PFC emulsions that contain perfluoro-15-crown-5-ether (green) and a lipid bilayer (pink). Twenty-one percent of oxygen corresponds to 160 mm Hg, and 100% of oxygen corresponds to 760 mm Hg.

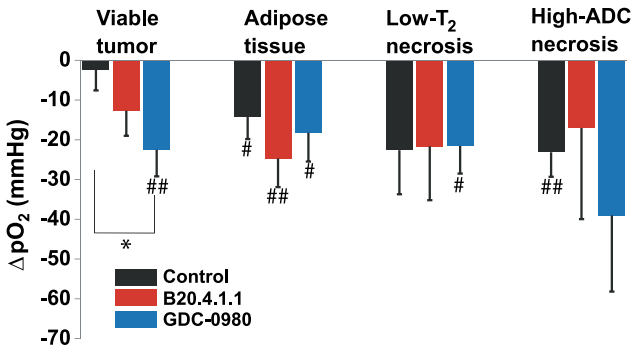

Figure W2. At 72 hours posttreatment, GDC-0980 significantly decreased pO_2 in the viable tumor but not in the other tissue classes when compared with the control group ($^*P < .05$), whereas the B20.4.1.1-treated group showed no significant differences relative to the control ($P > .05$). $^{\#}P < .05$ *versus* pretreatment; $^{\#\#}P < .01$ *versus* pretreatment level.